JoT JOURNAL OF TURBULENCE

http://jot.iop.org/

Sidewall boundary layer instabilities in confined swirling flow†

Hugh M Blackburn

CSIRO Building Construction and Engineering, PO Box 56, Highett 3190, Australia
E-mail: hugh.blackburn@dbce.csiro.au

Received 21 November 2000; online 2 May 2001

Abstract. We examine enclosed swirling transitional and turbulent flows in a cylindrical vessel, driven by a single rotating endwall. The cylinder height:radius ratio $H/R = 1$ was chosen explicitly to preclude the possibility of vortex breakdown on the cylinder axis, thus concentrating attention on the behaviour of the cylindrical sidewall boundary layers. Over a range of Reynolds numbers above $Re = \Omega R^2/\nu = 1 \times 10^4$, sidewall boundary layer instabilities evolve to form near-wall vortex structures that are aligned with the wall traction field. The number of structures increases with Reynolds number, and the characteristic length scale drops. A DNS study with matching LDV validation confirms the presence of near-wall vortex structures, which precess slowly around the container.

PACS numbers: 47.27.Nz, 47.15.Rq, 47.32.Cc.

† This article was chosen from selected Proceedings of the Eighth European Turbulence Conference (*Advances in Turbulence VIII (Barcelona, 27–30 June 2000)* (Barcelona: CIMNE) ed C Dopazo. ISBN: 84-89925-65-8).

 PII: S1468-5248(01)22929-4 1468-5248/01/000001+14$30.00

Contents

1. Introduction

The flow that is produced in a cylindrical container by a rotating endwall has been the subject of many studies, as it provides a convenient prototype for industrial and geophysical swirling flows. Much attention has been paid to aspects of axial vortex breakdown and stability at Reynolds numbers up to the onset of chaotic behaviour, but rather less attention to describing the characteristics of the flow after the onset of turbulence.

Some recent studies of rotating flows in low aspect ratio cylindrical containers with differential endwall rotation have indicated the presence of sidewall boundary layer instabilities. In physical experiments with a rotating cylindrical tank and rheoscopic fluid flow visualization, Hart and Kittelman [1] described and suggested possible mechanisms for a number of sidewall instabilities that appeared as the differential endwall co-rotation rate was raised. If the endwall rotates more slowly than the container, or counter-rotates slowly, the sidewall boundary layer flow is centrifugally stable. On the other hand, for sufficiently high differential rotation rates, a variety of instability structures arise. At the lowest differential rotation rates for which instabilities were noted by Hart and Kittelman, these take the form of axially-propagating axisymmetric rolls, progressing to stationary non-propagating helical rolls, through helical rolls with prograde rotation (i.e. rotating in the same sense as the differential rotation), to wavy vortices and turbulence at the highest differential rotation rates. Lopez [2], using unsteady axisymmetric simulations of rotating tank flows with differential endwall rotation, also observed some sidewall boundary layer instabilities that appear to propagate axially along the path where the axial velocity has a near-wall extremum. His simulation results show that for this case the wall-normal profile of the axial velocity is inflectional.

Here, we study flows in a stationary cylindrical cavity with a single rotating endwall, and find that sidewall boundary layer instabilities again arise. The observed instabilities take the form of localized flow separations, with the lines of separation aligned with the near-wall traction field. These structures move with a slow prograde rotation around the cylinder sidewall. In order to concentrate on the behaviour of sidewall boundary layer instabilities, without any possible interaction with axial vortex breakdown, the cylinder aspect ratio was selected to preclude flows

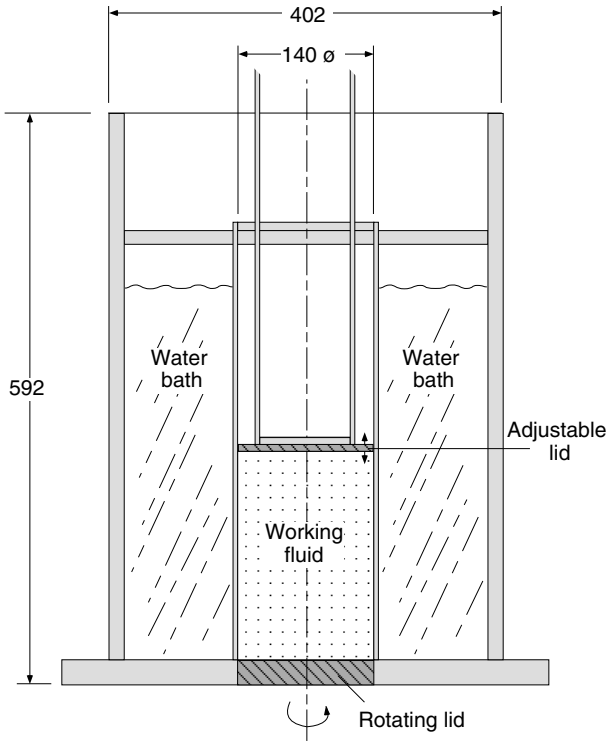

Figure 1. Diagram of experimental apparatus, dimensions in millimetres. All solid components shown, except rotating lid, are fabricated from clear acrylic plastics.

with vortex breakdowns on the cylinder axis; according to Escudier [3], no breakdowns are observed for values of $H/R \lesssim 1.2$, regardless of Re†.

The work presented here is for a cavity of height:radius ratio $H/R = 1$, with a Reynolds number range $Re = \Omega R^2/\nu = 1 \times 10^4$–$2 \times 10^5$. A single Reynolds number $Re = 2.5 \times 10^4$ was chosen for a detailed DNS and LDV investigation.

2. Experimental equipment and techniques

A diagram of the experimental apparatus is shown in figure 1. The rotating endwall/lid, made of polished stainless steel, is spun by a variable-frequency-drive four-pole electric motor through a V-belt coupling. The remainder of the rig was manufactured from clear acrylic sheet and tube: the enclosure of the outer water bath is a rectangular box. The working fluid was pure water. A more detailed description of the apparatus can be found in [5].

Flow visualization was carried out using two techniques. In the first, a small amount of rheoscopic fluid (supplied by Kalliroscope Corporation) was added to the working fluid, and global lighting was used. The micro-platelets in the fluid align with the local strain-rate field and by gradients in intensity of reflected light reveal flow structure near the wall. For the second technique, fluorescein dye was injected near the rotating wall through a retractable metal tube inserted through the upper stationary lid, and illuminated with argon-ion laser light.

† For a study of the transition to non-axisymmetry for an aspect ratio that allows axial vortex breakdown, see Blackburn and Lopez [4].

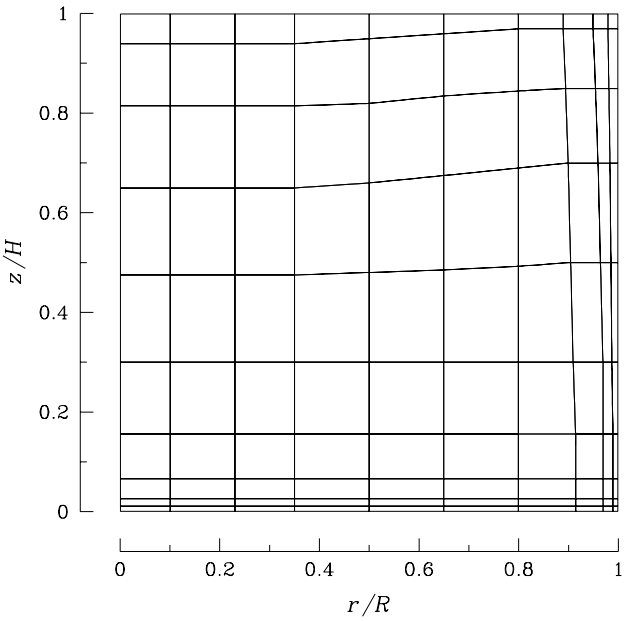

Figure 2. Spectral element mesh used to discretize the meridional semiplane. Cylinder axis to left, rotating endwall at bottom.

This lighting was arranged as two parallel sheets, one containing the cylinder axis, the other forming a short chord, nearly tangential to the outer cylindrical wall.

LDV measurements of time-mean azimuthal and axial velocities were obtained using a TSI 900-3 two-component system with a 600 mm focal length lens, traversed by a GMFanuc-Robotics S-10 industrial robot, with nominal positional accuracy 0.25 mm.

3. Numerical techniques

Numerical simulations were carried out using a cylindrical-coordinate spectral element–Fourier method, similar to that described by Tomboulides and Orszag [6], to solve the incompressible Navier–Stokes equations. The adoption of Fourier expansions in the azimuthal direction preserves the rotation symmetry of the equations, geometry and boundary conditions in the discretized system, and allows the radial and azimuthal velocities to be combined into two new variables that regularize the Navier–Stokes equations at the origin and decouple the viscous terms in the corresponding evolution equations [7]. The numerical method used here is identical to that employed in [4].

A mesh of 100 spectral elements was used to discretize the geometry in meridional semiplanes, as shown in figure 2. Mesh refinement was used to concentrate resolution near the rotating endwall, the adjoining stationary endwall, and in particular near their junction. Interpolation functions within each element were tensor products of Gauss–Lobatto–Legendre Lagrange polynomials, resulting in a standard spectral element method with no special numerical treatment at the axis, other than accommodation of the modal dependence of axis boundary conditions. At the Reynolds number employed in the computational part of the study ($Re = 2.5 \times 10^4$), ninth-order tensor-product interpolants (resulting in 8281 independent mesh points in the meridional semiplane) were found to adequately resolve the flow in an axisymmetric convergence investigation, and were used to obtain the numerical results presented here. A skew-symmetric formulation of the nonlinear terms is employed [8], and time integration is second

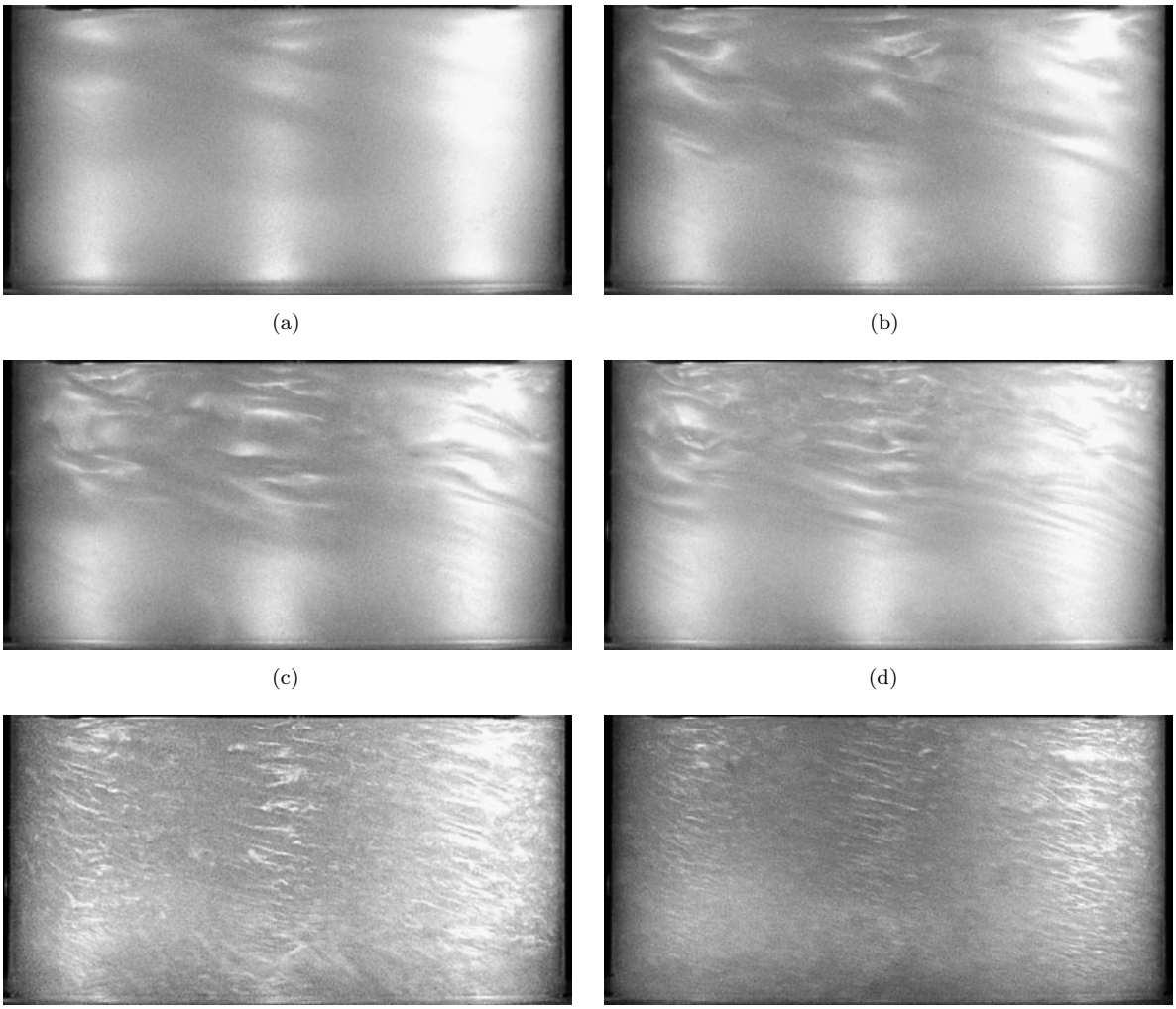

Figure 3. Rheoscopic fluid flow visualization, showing the effect of Reynolds number on near-wall flow features. In each image, the rotating wall is at the bottom and moves right–left nearest to the observer. The effect of three vertical diffuse bands of light results from three-spot illumination. (a) $Re = 1 \times 10^4$; (b) $Re = 2.5 \times 10^4$; (c) $Re = 3.75 \times 10^4$; (d) $Re = 5 \times 10^4$; (e) $Re = 1 \times 10^5$; (f) $Re = 2 \times 10^5$.

order, using the time splitting suggested in [9]. The numerical implementation is parallelized across two-dimensional Fourier modes, and not de-aliased in the azimuth.

4. Flow visualization

An array of rheoscopic fluid flow visualization photographs in figure 3 illustrates the effect of Reynolds number on the near-wall flow structure, as observed from a viewpoint normal to the cylinder axis. For all cases, the time-average near-wall flow follows approximately helical streamlines that lead bottom-to-top and right-to-left. At $Re = 1 \times 10^4$, some evidence of flow instability can be observed; by $Re = 2.5 \times 10^4$ the flow locally separates from the wall (see dye

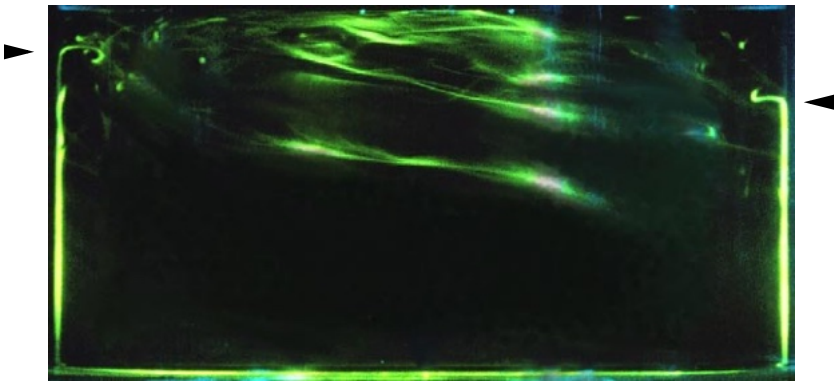

Figure 4. Fluorescein dye visualization at $Re = 2.5 \times 10^4$. The flow is lit by two parallel sheets of laser light, one containing the cylinder axis, the other forming a chord nearly tangential to the cylindrical wall. Arrowheads near the periphery indicate sections of near-wall flow separations, while in the centre, dye marks near-wall vortices.

visualization in figure 4) from $z/H \gtrsim 0.4$. As the Reynolds number is increased, the number of flow separation features increases, their characteristic length scales decrease, and the elevation at which they become apparent approaches the rotating endwall. The evidence suggests that the instabilities arise in the flow along the stationary cylindrical wall rather than on the rotating endwall.

A photograph of fluorescein dye visualization at $Re = 2.5 \times 10^4$ is shown in figure 4. As outlined in section 2, the flow is illuminated with two laser sheets, one containing the cylinder axis, the other forming a chord nearly tangential to the outer wall. Both were normal to the direction of view. Dye is injected near the intersection of the cylinder axis and the rotating wall through a retractable small-bore tube, and is advected to the cylinder wall, where it travels towards the stationary endwall. The photograph illustrates the flow at a time soon after the injection of dye, before it has advected back to the interior of the container. The diametral light sheet reveals local advection of dye away from the wall—two well developed eruptions are marked on the periphery of the figure. The glancing light sheet reveals elongated structures near the centre of the view; on the evidence of the diametral section and the rheoscopic flow visualizations of figure 3, these correspond to near-wall vortices. Similar structures have also been observed using an acid–base–indicator visualization method (not described in further detail here).

5. Results at $Re = 2.5 \times 10^4$

This section describes a dataset resulting from a direct numerical simulation carried out for $Re = \Omega R^2/\nu = 2.5 \times 10^4$. After axisymmetric flow was fully developed, a small random perturbation was added to the fundamental Fourier mode, and the flow evolved until a statistically steady state was reached. Following this, collection of statistical data was initiated. A check of azimuthal resolution verified that the primary spectral statistics and time-average velocity profiles were very similar for both 96 and 128 planes of data in the azimuth; results presented here are for the 96-plane simulation.

JoT 2 (2001) 009

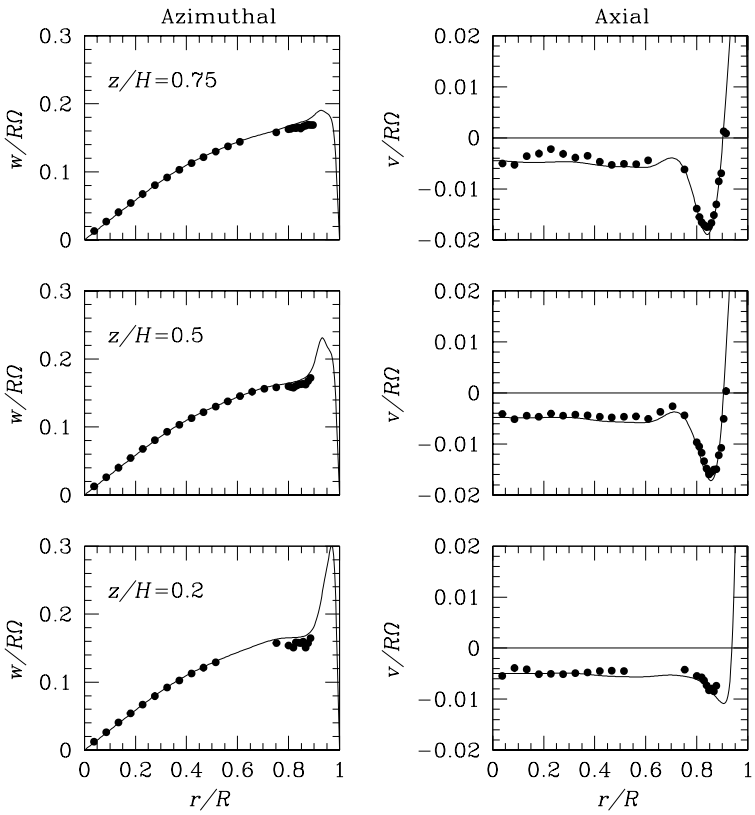

Figure 5. A comparison of computed (——) and measured (•) time-mean flow at three axial locations for $Re = \Omega R^2/\nu = 2.5 \times 10^4$.

5.1. Comparison to LDV measurements

A comparison of measured and computed time-mean azimuthal and axial velocity profiles at three axial locations is presented in figure 5. The near-wall LDV measurements are unreliable, owing to a lack of spatial resolution, and have been omitted. However, the generally good agreement between the computed and measured results may be noted. A feature apparent in the velocity profiles is the presence of a cylindrical wall jet, which results from the diversion of the boundary layer formed on the rotating endwall. This jet flow is strongest and sharpest near the rotating endwall, and becomes weaker and more diffuse near the stationary endwall. The profiles for both velocity components are inflectional and satisfy the requirements for inviscid shear flow instability; in addition, the outer segments of the azimuthal velocity profiles satisfy the requirements for inviscid centrifugal instability (see [10], sections 15 and 22).

5.2. Instantaneous data

All results presented in this section derive from the same instantaneous velocity field. The axial, radial and azimuthal velocity components are denoted by u_z, u_r and u_θ respectively.

A view of instantaneous contours of axial velocity on near-wall ($z/H = 0.998$, $r/R = 0.998$) surfaces is shown in figure 6. This reveals the presence of flow reversals near the cylindrical wall. The regions of reversal are approximately aligned with the time-mean cylindrical wall streamlines, i.e. with the integral curves of the time-mean wall traction field. Although there is strong evidence of quasi-regular structure, the random nature of the contours, particularly on the top wall, indicates that the flow is weakly turbulent.

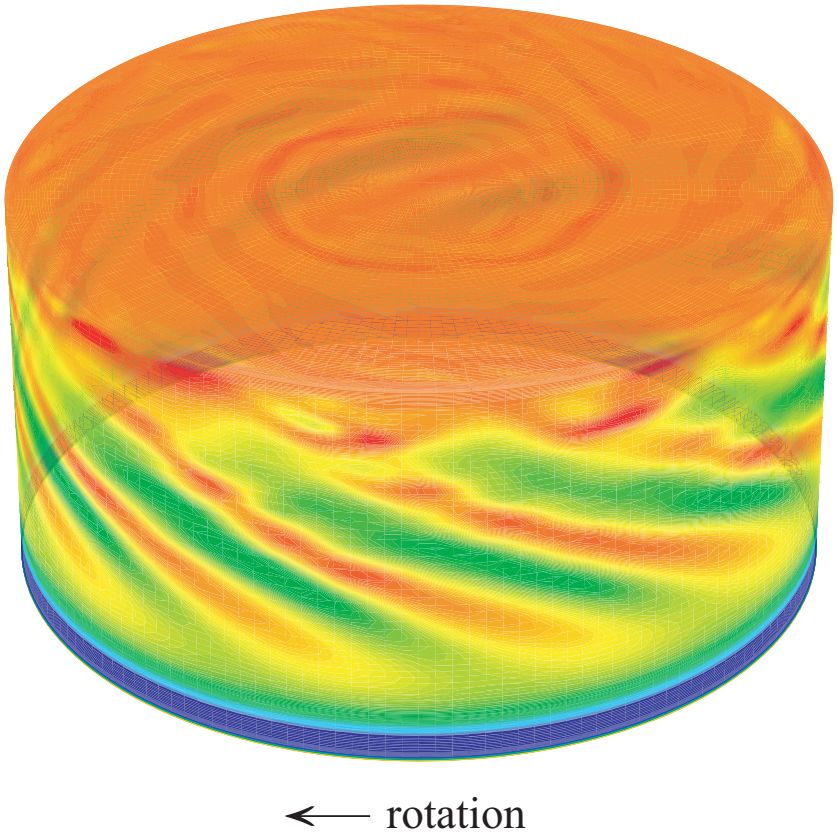

Figure 6. Instantaneous contours of axial velocity on near-wall surfaces. The rotating endwall is at the bottom, with the sense of rotation as indicated.

Figure 7 shows an instantaneous isosurface of strain-rate magnitude $\gamma = (2\boldsymbol{S}{:}\boldsymbol{S})^{1/2}$ where $\boldsymbol{S}$ is the symmetric rate-of-strain tensor $\boldsymbol{S} = 0.5\left[\nabla\boldsymbol{u} + (\nabla\boldsymbol{u})^t\right]$. The ten structures thus revealed near the cylindrical wall are related to the regions of flow reversal shown in figure 6. Examination of similar isosurfaces computed at different points in time show there to always be ten structures, moving with a slow prograde rotation (in the same sense as the rotating lid), at a rate $\omega/\Omega \approx 0.09$.

Approximations to the instantaneous wall streamlines—integral curves in the velocity fields interpolated onto surfaces at distances $0.0005R$ from the container's wall—are shown in figure 8. A developed view of the instantaneous cylindrical wall streamlines shown in figure 8(b) is replotted in figure 9; this shows more clearly the approximately regular alternation of negative and positive streamsurface bifurcations (for an extended treatment of the topological terms used here, consult Hornung and Perry [11]). On an azimuthal traverse there are ten open negative streamsurface bifurcations, which are lines to which wall streamlines converge, and where material departs from the wall. These are observed to form at elevations $z \gtrsim 0.4H$. The extreme regularity of the wall streamlines at smaller elevations supports the idea that the near-wall flow relaminarizes on the rotating endwall, and becomes unstable on the cylindrical wall.

The negative streamsurface bifurcations produce eruptions of material from the wall, as follows from continuity, and as shown in the dye visualization of figure 4. A view of instantaneous sectional streamlines [11] on an axial–radial section through a negative streamsurface bifurcation is shown in figure 10. Between the separation sectional streamline and the wall lies another

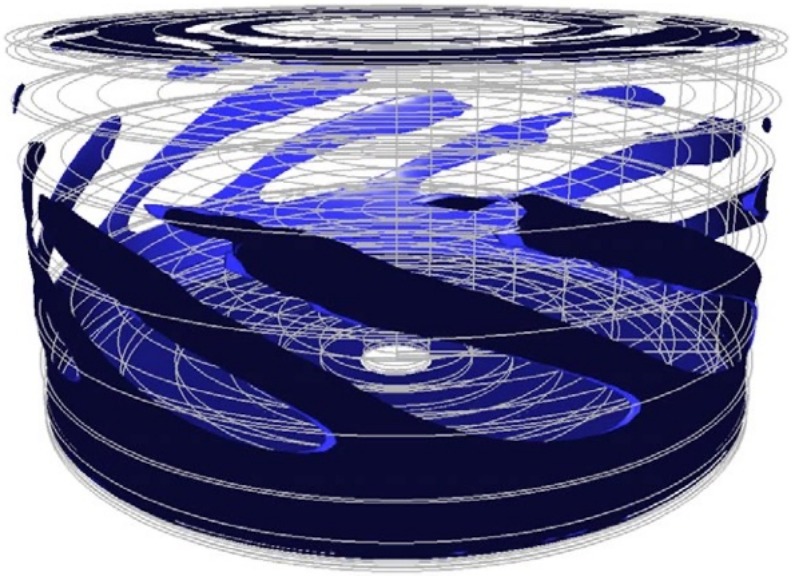

Figure 7. Instantaneous isosurface of strain-rate magnitude γ.

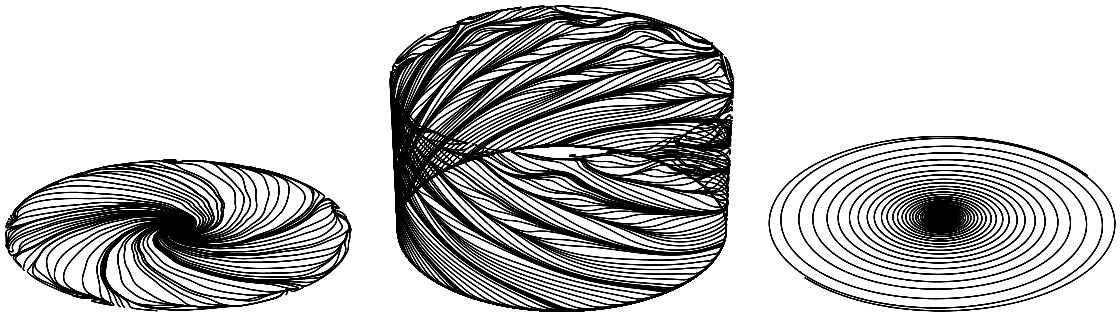

(a) (b) (c)

Figure 8. Approximations to the instantaneous wall streamlines on: (a) fixed endwall; (b) cylindrical wall; (c) rotating endwall.

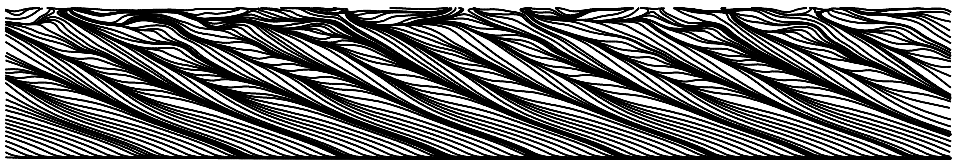

Figure 9. Approximations to the instantaneous wall streamlines on a developed view of the cylindrical wall.

local flow reversal and a reattachment sectional streamline; this separation–reattachment pair corresponds to a negative–positive streamsurface bifurcation pair.

Figure 11 shows instantaneous sectional streamlines and contours of Reynolds stress components $u'_z u'_r$ and $u'_z u'_\theta$ in a meridional semiplane. Two sectional streamline separation features are tagged in figure 11(a); these are seen in figure 11(c) to correspond to pairs of local instantaneous $u'_z u'_\theta$ extrema.

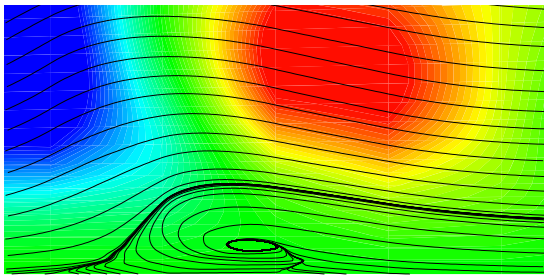

Figure 10. An example of instantaneous sectional streamlines (computed using the axial and radial velocities) on an axial–radial section through a negative streamsurface bifurcation. The view has the cylindrical wall aligned horizontally and shows a region $0.08H \times 0.04R$. Colour contours are of radial velocity.

5.3. Statistical data

The statistics presented here were collected over a period of approximately 30 endwall revolutions, after the simulation had reached a statistically steady state (as assessed from an examination of time series of Fourier modal energies).

Figure 12 shows the azimuthal energy spectrum, revealing significant energy in the 10th wavenumber and its harmonics, embedded in a monotone background energy spectrum. The (instantaneous) energy in each azimuthal Fourier mode k is given by

$$E_k = \frac{1}{2A}\rho \int_A \hat{\boldsymbol{u}}_k \cdot \hat{\boldsymbol{u}}_k^* r \, \mathrm{d}A$$

where A is the area of the two-dimensional meridional semiplane, ρ is the fluid density, r is the distance from the axis and $\hat{\boldsymbol{u}}_k^*$ denotes the complex conjugate of the velocity data in the kth Fourier mode. The energy of the axisymmetric base flow is represented by E_0, and its dominance of the spectrum reveals that the vast majority of the flow kinetic energy resides in the axisymmetric component. By inference it is the presence of ten flow-separation features exemplified in figures 6–9 that gives rise to the spectral peaks at the $10n$ harmonics shown in figure 12.

The strongest reversed flow is also the site of the highest axial–azimuthal Reynolds stress, which peaks at $r/R \simeq 0.95$, $z/H \simeq 0.5$, as shown in figure 13. The flow separations produce most of the turbulent momentum transport in this flow. Close examination of the time-mean sectional streamlines, also shown on figure 13, reveals a small separation zone around the junction of the cylindrical and stationary end walls.

5.4. Axisymmetric flow

It is interesting to compare the three-dimensional DNS results to those found using axisymmetric computations. Here, in figure 14, we present just one example from an axisymmetric simulation at $Re = 2.5 \times 10^4$, in the form of instantaneous sectional streamlines. The interesting feature is that while obvious signs of instability are observed in the wall-jet flow near the cylindrical wall, no flow separation takes place—the instability is manifest in the form of axisymmetric waves. Thus the flow separation features observed in the physical experiments and the full DNS require a breakage of axisymmetry.

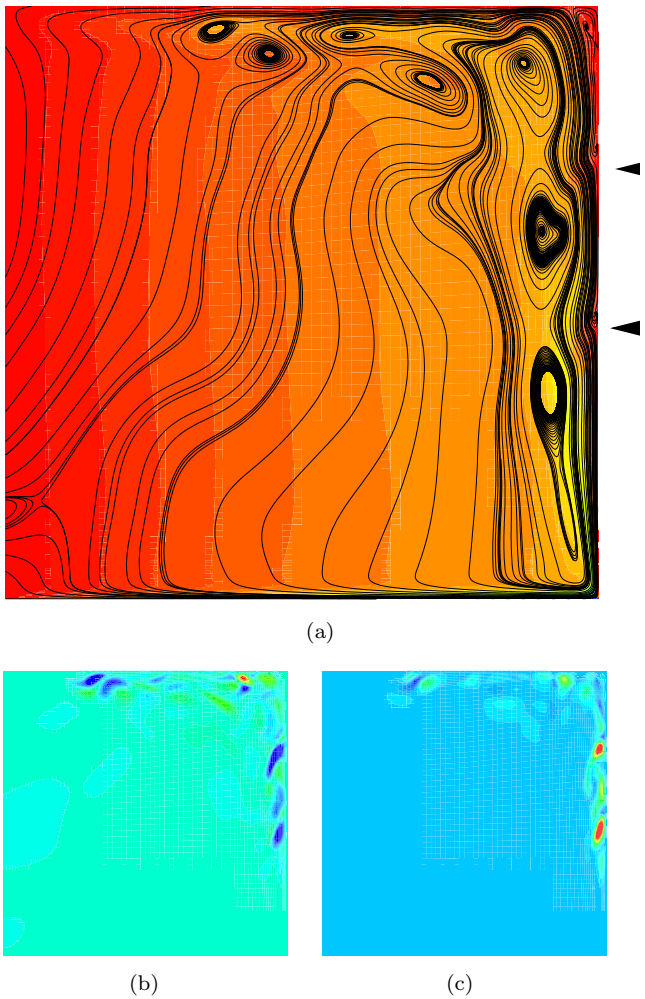

Figure 11. Co-instantaneous flow features on a meridional semiplane: (a) sectional streamlines over background contours of azimuthal velocity, with wall separations indicated; (b) Reynolds stress $u'_z u'_r$; (c) Reynolds stress $u'_z u'_\theta$. In each view, the axis is to the left, the rotating endwall at the bottom.

6. Discussion and conclusions

This study of transitional flow in a cylindrical cavity driven by a rotating endwall notes the presence of sidewall boundary layer instabilities that give rise to localized flow separations on the cylindrical wall. The instabilities of the cylindrical wall boundary layer could be of either shear flow or centrifugal type. The flow separations are shown to be associated with vortex structures that lie very close to the cylindrical wall of the container. These boundary layer structures are aligned with the time-mean wall traction field, and have the appearance of an array of helices that has a slow prograde rotation.

At the single Reynolds number selected for detailed investigation, there is good agreement between the computed and measured time-mean flow fields, and qualitative agreement between the features of the computed and flow visualization results. The computed results do, however, appear to be more regular. For example, the flow visualization results presented in figure 3(b) for $Re = 2.5 \times 10^4$ do not suggest an equispaced array of flow separation features as observed in

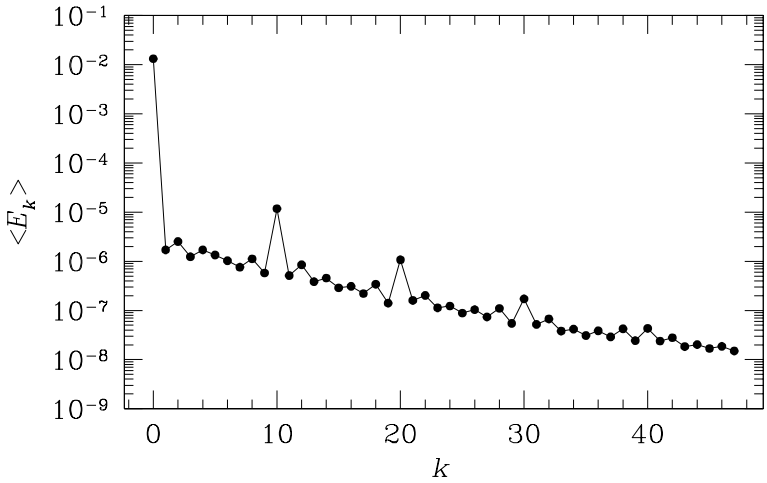

Figure 12. Spectrum of azimuthal modal energies at $Re = 2.5 \times 10^4$.

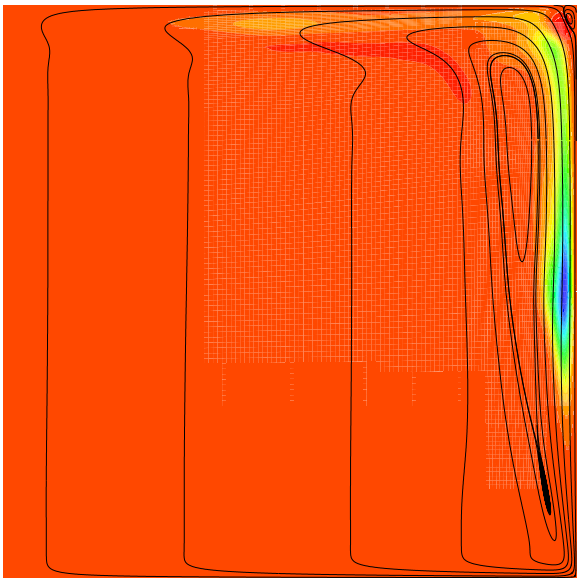

Figure 13. Contours of axial–azimuthal Reynolds stress component $\langle u'_z u'_\theta \rangle$ in a meridional semiplane, overlaid with time-mean sectional streamlines.

the computed results of figures 6 and 7. This difference is presumably caused by the presence of geometric imperfections and boundary condition noise in the physical experimental set-up, for example small fluctuations in speed of the rotating endwall.

The union of the surface streamline fields in figure 8 provides the surface streamline field on the cylindrical boundary of the flow, which is a simple manifold. A close inspection reveals ten node/focal features (including the two axial foci) and eight saddles, a difference of two, as required by the Poincaré–Bendixson theorem (see Perry and Chong [12] and Lighthill [13], section 2.7).

The physical situation investigated here, with flow in a stationary cylindrical container with a single rotating endwall, represents a subset of the rotating tank/co-rotating endwall

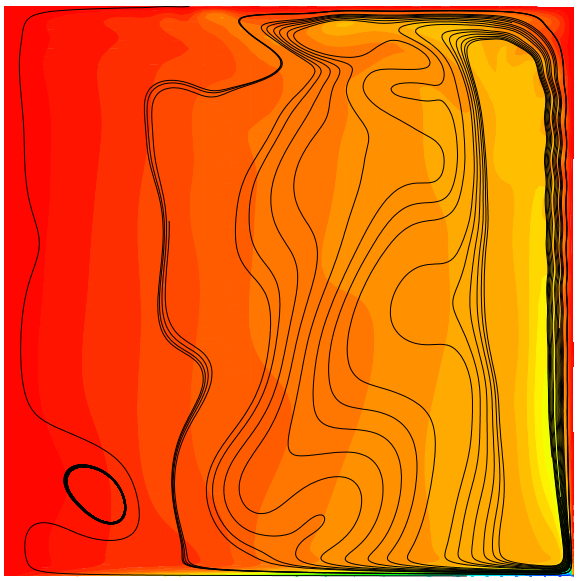

Figure 14. Instantaneous sectional streamlines for an axisymmetric simulation at $Re = 2.5 \times 10^4$. Background colour contours are of azimuthal velocity.

experiments of Hart and Kittelman [1]. At low differential rotation rates (low Rossby numbers), Hart and Kittelman observe what appear to be axially-propagating axisymmetric rolls, but at high Rossby numbers they observed instabilities with helical structure and prograde propagation; those features appear related to the flow separations noted in the present work.

In another study, Blackburn and Lopez [4] examine the onset of symmetry-breaking behaviour for Reynolds numbers $Re \gtrsim 3000$, and for a cylinder aspect ratio $H/R = 2.5$ that does not preclude vortex breakdown on the cylinder axis. There, symmetry-breaking bifurcations were found to take the form of rotating waves, at wavenumbers $k = 5$ and $k = 6$, modulated in time by the underlying axisymmetric flow behaviour. The maximum wave energy is not associated with a precession of the vortex core but instead appears to be associated with an instability of the cylindrical wall-jet; the peak wave kinetic energy arises near $r/R = 0.67$, $z/H = 0.8$. The waves have a slow prograde rotation speed that is close to the mean angular velocity at that location.

Given the variation in cylinder aspect ratio (2.5 versus 1) and the order-of-magnitude difference in Reynolds numbers between the work presented in [4] and that studied in detail here, it is obviously difficult to draw a strong connection between the observed behaviours at this stage. Some similarities, however, are notable: first, that the symmetry-breaking structures in both cases are associated with a wall-jet flow that appears to have an inflectional instability; secondly, these structures have a slow prograde precession around the cylinder. One might expect that as Reynolds numbers increase and the radial thickness of the wall-jet reduces, the characteristic length scale of the instability would fall, with an associated rise in characteristic wavenumber, as is consistent with this comparison.

Experimental flow visualization studies conducted over a range of Reynolds numbers and cylinder aspect ratios (flows for aspect ratios other than $H/R = 1$ have been investigated but are not dealt with in detail here) suggest that the near-wall vortical structures with local separation are a characteristic feature for this flow after the onset of turbulence—they maintain alignment with the wall traction field, but become smaller and more numerous, and are evident closer to the rotating endwall as the Reynolds number increases, indicating law-of-the-wall type scaling.

This could be expected in the inner-layer velocity profile that lies between the peak wall-jet flow speed and the cylindrical wall [14].

Acknowledgments

The author gratefully acknowledges the assistance of Belinda Wadeson, John Sheridan of Monash University and Lawrence Cheung of CSIRO in preparing the flow visualization images presented here.

References

[1] Hart J E and Kittelman S 1996 Instabilities of the sidewall boundary layer in a differentially driven rotating cylinder *Phys. Fluids* **8** 692–6
[2] Lopez J M 1998 Characteristics of endwall and sidewall boundary layers in a rotating cylinder with a differentially rotating endwall *J. Fluid Mech.* **359** 49–79
[3] Escudier M P 1984 Observations of the flow produced in a cylindrical container by a rotating endwall *Exp. Fluids* **2** 189–96
[4] Blackburn H M and Lopez J M 2000 Symmetry breaking of the flow in a cylinder driven by a rotating endwall *Phys. Fluids* **12** 2698–701
[5] Stokes J R, Graham L J W, Lawson N J and Boger D V 2001 Swirling flow of viscoelastic fluids. Part 1. Interaction between inertia and elasticity *J. Fluid Mech.* **429** 67–115
[6] Tomboulides A G and Orszag S A 2000 Numerical investigation of transitional and weak turbulent flow past a sphere *J. Fluid Mech.* **416** 45–73
[7] Orszag S A 1974 Fourier series on spheres *Mon. Weather Rev.* **102** 56–75
[8] Zang T A 1991 On the rotation and skew-symmetric forms for incompressible flow simulations *Appl. Num. Math.* **7** 27–40
[9] Karniadakis G E, Israeli M and Orszag S A 1991 High-order splitting methods for the incompressible Navier–Stokes equations *J. Comput. Phys.* **97** 414–43
[10] Drazin P G and Reid W H 1981 *Hydrodynamic Stability* (Cambridge: Cambridge University Press)
[11] Hornung H and Perry A E 1984 Some aspects of three-dimensional separation, part I: streamsurface separations *Z. Flugwiss. Weltraumforsch.* **8** 77–87
[12] Perry A E and Chong M S 1987 A description of eddying motions and flow patterns using critical point concepts *Ann. Rev. Fluid Mech.* **19** 125–55
[13] Lighthill M J 1963 Introduction. Boundary layer theory *Laminar Boundary Layers* ed L Rosenhead (Oxford: Oxford University Press) ch 2, pp 46–103
[14] Launder B E and Rodi W 1983 The turbulent wall jet—measurements and modeling *Ann. Rev. Fluid Mech.* **15** 429–59